The Astrophysical Journal, 897:68 (8pp), 2020 July 1 https://doi.org/10.3847/1538-4357/ab908b

Solar Filaments and Interplanetary Magnetic Field B_z

V. Aparna and Petrus C. Martens
Department of Physics & Astronomy, Georgia State University, Atlanta, GA 30303, USA; aparna@astro.gsu.edu
Received 2019 August 30; revised 2020 April 29; accepted 2020 May 4; published 2020 July 2

Abstract

The direction of the axis of an interplanetary coronal mass ejection (ICME) plays an important role in determining if it will cause a geomagnetic disturbance in the Earth's magnetosphere upon impact. Long period southward-pointing ICME fields are known to cause significant space weather impacts and thus geomagnetic storms. We present an extensive analysis of CME–ICME directionality using 86 halo-CMEs observed between 2007 and 2017 to compare the direction of the source filament axial magnetic field on the Sun and the direction of the interplanetary magnetic field near the Earth at the L1 Lagrangian point. Excluding 12 cases that were too ambiguous to determine, for the remaining 74 ICMEs, we find an agreement in terms of the northward/southward orientation of B_z between ICMEs and their CME source regions in 85% of cases. Some of the previous studies discussed here have obtained an agreement of 77% and 55%. We therefore suggest that our method can be meaningful as a first step in efficiently predicting geoeffective ICMEs by observing and analyzing the source regions of CMEs on the Sun.

Unified Astronomy Thesaurus concepts: Solar filaments (1495); Space weather (2037); Solar coronal mass ejections (310)

1. Introduction

Monitoring space weather becomes increasingly important as human activities in space become routine. Effective measures must be taken to mitigate the impact due to explosive events from the Sun to protect power grids, spacecraft, satellites, and future astronauts to and from the Moon and on interplanetary voyages. The solar and space weather community uses various techniques to predict the effects of solar explosive events. Coronal mass ejections (CMEs) are monitored using coronagraphs such as the Solar and Heliospheric Observatory/Large Angle and Spectrometric Coronagraph (SOHO/LASCO; Brueckner et al. 1995). Modeling efforts like WSA-Enlil (Pizzo et al. 2011) strive to obtain precise arrival times of Earth-bound CMEs and/or corotating interaction regions (CIRs). While it is important to know when a CME occurs and how soon it will arrive at Earth, it is equally important to know if it will actually affect Earth and cause a geomagnetic storm. In this work we attempt to understand if the orientation of the axial magnetic field component (B_z) of interplanetary CMEs (ICMEs) near Earth can be predicted by monitoring solar source regions of the CMEs.

Several studies have been conducted in order to obtain the magnetic configuration of the CME source regions on the Sun. Yurchyshyn et al. (2001) used potential field modeling for two active regions that produced Earth-affecting CMEs and determined their helicities. They also calculated the helicities of the interplanetary magnetic field (IMF) at L1 corresponding to these eruptions using the Advanced Composition Explorer (ACE; Stone et al. 1998). Marubashi (1997) studied 12 magnetic clouds (MCs) to infer their axial field directions and compared them with the orientations of nine associated disappearing filaments on the Sun. In both the above studies, the authors find that the orientations of the MC axis match with the orientations of the axes of the associated active region or the disappearing filaments, respectively, on the Sun. Bothmer & Schwenn (1998) found that eight out of nine ICMEs retained the helicities of their source regions. Marubashi et al. (2015) conducted an analysis on the relation between the orientation of the filaments on the disk of the Sun and the corresponding storm-causing flux ropes at L1 using flux rope fitting models. Yurchyshyn (2008) performed a comparison of the MC axis for 25 cases using ACE data and the orientation of the post-flare arcades at the solar source using Extreme ultraviolet Imaging Telescope (EIT) images. Palmerio et al. (2018) have analyzed 20 CME–ICME pairs between 2010 and 2015 using chirality to find the flux rope type of the source region and coronal dimmings to find the axis direction of the flux rope.

It is well known that long periods of southward-pointing axial field of MCs or the IMF (B_z) will produce a significantly effective geomagnetic storm (Dungey 1962; Marubashi 1997; Gopalswamy et al. 2008). Because CMEs are known to have flux ropes in interplanetary space (Vourlidas et al. 2013), they must have definite magnetic structure, which can be utilized for the predictions of the field orientation (Gopalswamy et al. 2009). Knowing the axis direction of the source region on the Sun and hence the direction of the vertical component, is useful in estimating whether a CME event from the region will cause a geomagnetic storm. In the current work, we focus on determining the axial field direction of the CME source regions by observationally determining their chirality and correlating it with their ICME counterparts at L1.

Chirality is traditionally determined for Hα filaments using the orientation of the filament barbs with reference to the magnetic polarity inversion line (PIL), the direction in which the tail of the fibrils adjacent to the filament or the filament channel point, or by using the skew of post-flare arcade loops (Martin 1998). Once the handedness is determined, the direction of the filament axial field can be found with the aid of line-of-sight (LOS) magnetograms. For a list of halo-CMEs in this study, the enhancement in the IMF B_z direction is compared with the axis direction of the CME source region on the Sun.

While there have been several studies relating filaments and IMF such as the ones referenced above, the present study is more extensive, relating the two by using a simpler,

straightforward method of finding chromospheric filament chirality to get the axial magnetic field direction and the sign of IMF B_z. More importantly, we show that observables such as chirality of chromospheric filaments can be used for determining the geoeffectiveness of solar eruptions, which is important in order to avoid taking precautionary measures when not required. Furthermore, training machine-learning models to detect the chirality can help automate this process. Feature tracking algorithms that are already in use for tracking filaments and identifying sigmoids (Martens et al. 2012) can be developed for automatically detecting chirality. This will prove beneficial, as will be shown in this paper, for doing the predictions.

We give a brief account of the data and the methods we use in the next section. Section 3 describes the methodology of correlating source regions with IMF data. The results are given in Section 4. In Section 5, we compare our results with some of the studies mentioned above and give our conclusions.

2. Data and Methods

Halo-CMEs from 2007 to 2017 are analyzed for this study to find correlations between the axial magnetic field direction of eruptive regions on the Sun and the IMF. The list of CMEs during this period has been obtained from the Coordinated Data Analysis Workshop (CDAW)[1] list of halo-CMEs (Gopalswamy et al. 2009). Chiralities of filaments in the source location of eruptive regions on the Sun are obtained using solar images in Hα from the Global Oscillations Network Group (GONG; Harvey et al. 2011) and Kanzelhöhe Observatory (KSO; Pötzi et al. 2015). Chirality is determined mainly using the rules established by Martin (1998, 2015) and Martin et al. (2008). For quiescent filaments the spatial resolution of GONG, which is two arcsec per pixel in a 2048 × 2048 frame or 1.″02 in KSO, is quite enough to visually distinguish between a left-handed (i.e., sinistral) or right-handed (i.e., dextral) chirality filament, either by using barbs or by using fibrils adjacent to the filament. For active region filaments, neither barbs nor fibrils can be resolved using GONG or KSO. Where barbs or fibrils cannot be used for identifying the chirality, the orientation of the overlying potential arcade magnetic field is used for obtaining the direction of the axial magnetic field along the PIL (see Figure 1 in Martin 1998).

An example of each of the three methods discussed above for determining chirality is shown in Figure 1. Figure 1(a) shows a filament whose chirality can be found using the orientation of its barbs. Although filament barbs are used commonly to find the chirality, on some occasions barbs are not visible or are not present (common in active region filaments). In such cases, fibrils in the filament channel (Figure 1(c)) or post-flare arcades (Figure 1(e)) can be used effectively to determine the chirality. Fibrils adjacent to the filament spine have similar directionality as the barbs. Looking from the positive polarity, the tails of the fibrils of a dextral filament point away from the viewer. Images of active regions can get easily saturated in ground-based images due to high activity and so neither barbs nor fibrils can be used to find their chiralities. These regions may or may not have Hα filaments but they do always have a PIL. In most of these cases, the skew of the overlying arcade loops, usually clearly seen in the 171 Å channel of Solar Dynamics Observatory (SDO)/Atmospheric Imaging Assembly (AIA; Lemen et al. 2012), after the flare can be used to obtain the axial field direction of the PIL (see Figure 1(e)). Because the post-flare arcade loops are almost potential in nature, they can be used to understand the orientation of the ejecta. In all the above cases, magnetic polarity information (shown in Figures 1(b), (d), and (f) corresponding to (a), (c), and (e)) using at least LOS magnetograms is required to determine the direction of the axis. For the CME sources prior to 2010, SOHO EIT (Delaboudinière et al. 1995) 171 Å images along with Michelson Doppler Imager (MDI; Scherrer et al. 1995) magnetograms are used, while SDO/AIA data and Helioseismic Magnetic Imager (HMI; Scherrer et al. 2012) magnetograms are used post 2010.

The near Earth IMF is detected using magnetic field parameters from the ACE magnetometer and plasma parameters from the Solar Wind Electron Proton and Alpha Monitor (McComas et al. 1998) aboard ACE. These parameters are selected and plotted using the CDAWeb Data Explorer (NASA CDAWeb Development Team 2019). The details about deriving the various parameters in the CME catalog are given in Gopalswamy et al. (2009). The first two columns of this catalog denote the date and time at which the CME first appears in the LASCO C2 Coronagraph. The third and fourth columns give the apparent and space speed or the actual speed. The space speed is considered for our expected arrival time calculations with buffer time to account for accelerating and decelerating CMEs. Most CMEs take one to six days to reach Earth after the eruption. The CME travel time is calculated linearly for a rough estimate of the expected arrival time. However, we use the acceleration information in the fifth column of the catalog to qualitatively assess the actual speed of the CME and its arrival time.

We conduct our study using the north–south component of the axial magnetic field of the filaments in the CME source regions on the Sun. This is compared with the sign of the ICME Bz values recorded by ACE situated at the L1 Lagrangian point using the estimated arrival time of the CME. The analysis is done in the geocentric solar ecliptic coordinate system (Hapgood 1992). Along with a reasonable estimate of the arrival time of the CME, plasma parameters including B-total, B_z, solar wind velocity, proton density, temperature, and the disturbance storm-time (Dst) index are used for evaluating the signatures and effect of the ICME on the Earth's magnetosphere.

CME occurrences, their onset times, and nature (halo, partial halo, etc.) are visually confirmed with the help of JHelioviewer (Müller et al. 2009) by simultaneously observing the events in SDO/AIA and HMI channels along with the SOHO LASCO C2/C3 Coronographs. CMEs originating from behind the disk are ignored for this study. In cases of unavailability of magnetogram data or Hα data or when the source is close to the limb, data from a few days earlier or later when the region is on the disk (preferably between −45° and 45° longitude) are used to avoid inaccuracies in estimating the chirality due to the viewing angle projection effects. This is based on a reasonable assumption that the filament chirality does not change with time.

The onset times of the CMEs are important for obtaining reasonable arrival time estimates at Earth. About 1 to 10 CMEs occur per day. However, unless it is a CME with a wide angular width and sufficient speed, it is unlikely to impact the Earth's

[1] cdaw.gsfc.nasa.gov/CME_list/halo/halo.html

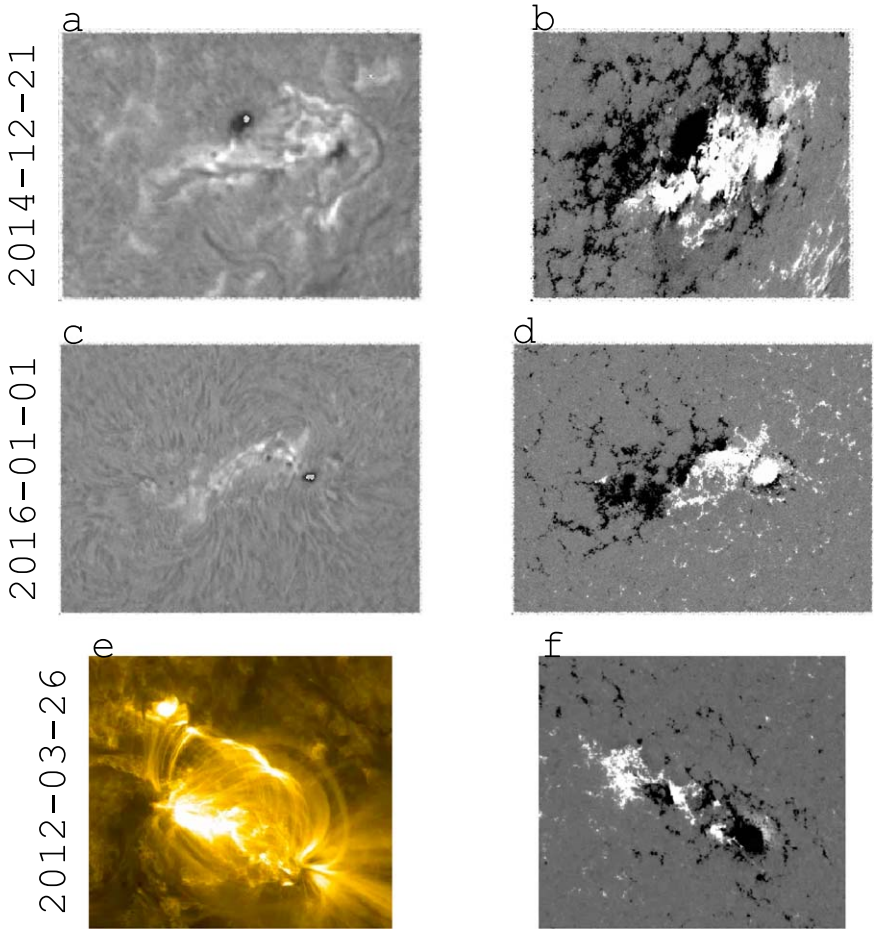

Figure 1. Examples for obtaining chirality and axial field of the region using the methods of Martin (1998). Panels (a) and (b) show GONG Hα and the corresponding HMI LOS magnetogram (NOAA AR #12242). The example is used to depict the orientation of barbs with respect to the PIL that can be identified in panel (b). Panel (a) has visible barbs that are pointing to the right making it a dextral filament. Fibrils in panel (c) are used along with the polarities from panel d (NOAA AR #12473,) to get a northwest pointing filament axis. Panel (e) shows post-flare arcade loops whose footpoint polarities are shown in panel (f) (N18W29).

magnetosphere. Hence, analyzing CMEs from the Halo-CME list, which is a subset of all the CMEs, is deemed sufficient. However, in certain cases, as will be discussed in the next section, the CME arrival time does not match with time of the ICME signatures near Earth, and in some cases there are several CME signatures in the IMF. In these cases the CME catalog consisting of all the CMEs is consulted for one or two days before and after the day of interest in order to assess if those signatures result from other CMEs. Furthermore, the flare class, Measurement Position Angle and acceleration columns are left as such in our catalog for making them all available in one place for possible future studies. This study contributes to this database the 10th, 11th, and 12th columns that give the IMF B_z obtained by the analysis of the ACE plots, the axial magnetic field direction, and the chirality of the source region derived from the analysis of observed filaments, respectively. The list of ICMEs used for this study, including our results, are available at Harvard Dataverse (10.7910/DVN/QBQFXA). The following section explores in detail some of the events.

3. Analysis

CMEs originate as singular eruptions on the Sun but as they travel through the interplanetary space they may interact with other disturbances (CMEs or CIRs). There may be one or multiple CME signatures near Earth (e.g., Figure 2), signatures of CIRs (e.g., Figure 3) caused by the interaction between fast and slow solar wind regions or a combination of these making it a challenge to correctly identify what caused which structure and relate them to their source regions on the Sun. In order to consistently identify the features we adhere to certain criteria that have been previously adapted by Gopalswamy (2009), Forsyth & Marsch (1999), Burlaga et al. (1981), etc. We briefly discuss these criteria below.

Depending on the viewing angle of the spacecraft, it may or may not see an MC (i.e., a flux rope) in the three-part CME structure. The most common features for identifying a CME near the Earth, commonly called ICME, are the enhancement in the total magnetic field and an abrupt increase in the solar wind speed indicating a fast shock wave, temperature, and pressure. The effects of an ICME may last for a few hours up to a few days. In the ICME structure the sheath region between the shock-front and the ICME volume is indicated by rapidly varying magnetic field prior to its enhancement (Kilpua et al. 2017 and references therein). The MC is indicated by the enhancement in the total magnetic field that decreases gradually over the time of passage of the CME through the spacecraft (indicated in Figure 2). In cases of CIRs, there are typical mesa (table-like) or inverse mesa-like structures (indicated in Figure 3) in the proton density, velocity, and alpha-particle-to-proton ratio profiles (not shown in the figure; Burlaga et al. 1981).

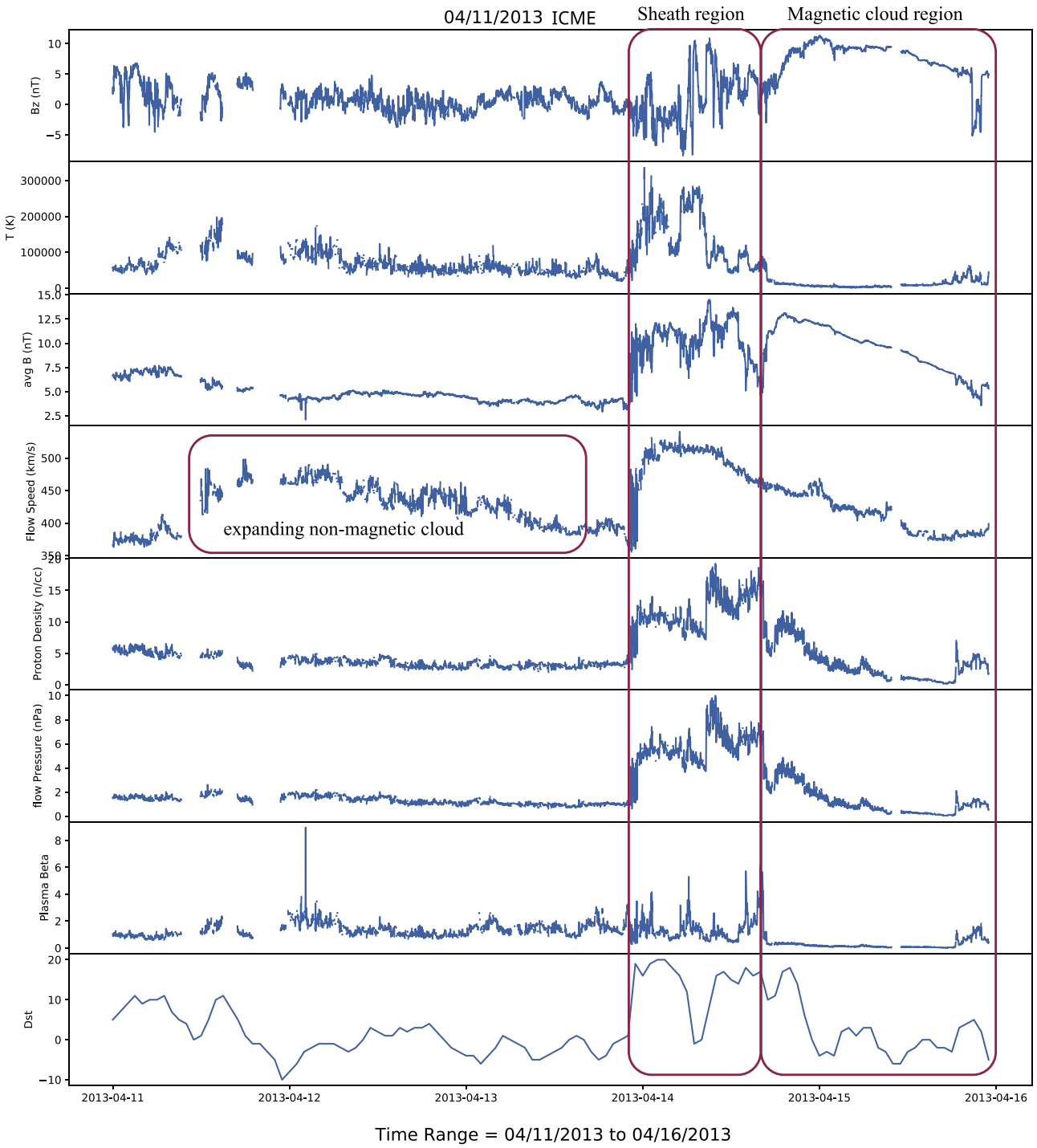

Figure 2. Example of solar wind containing at least one ICME structure with a northward enhancement as seen in the *Bz* panel. Flow speed, density, and pressure show a gradual decrease indicating an expanding ICME. The boxed region on the left shows an example of the signature of a non-MC. The boxed region on the right depicts the duration of the sheath region and the CME at L1.

Strong or long-lasting southward-pointing ICME magnetic fields have the largest effects on the Earth's magnetosphere. We observe the enhancement in the B_z component of the ICME magnetic field associated with the CME source region on the Sun. The associated region on the Sun that produced the CME is determined using the time when it was first observed by the LASCO C2 Coronagraph on SOHO and the flare onset time and location as recorded in the CDAW catalog. The ejection is visually confirmed by observing coronal dimming, post-flare arcade loops and/or filament eruptions.

In order to ensure that an Earth-bound CME corresponds to a particular ICME, we check for other CMEs within ± 2 days from that date. Halo-CMEs are more likely to cause fluctuations in the Earth's magnetosphere compared to partial-halo CMEs. Narrow and slow CMEs have very low probability of causing an appreciable impact. In almost all cases in our study, nonhalo CMEs were of angular width less than 60° and slow ($<500\,\mathrm{km\,s^{-1}}$), and thus are reasonably considered as poor events in the CME catalog. Furthermore, arrival estimates for CMEs match with the ICME signatures.

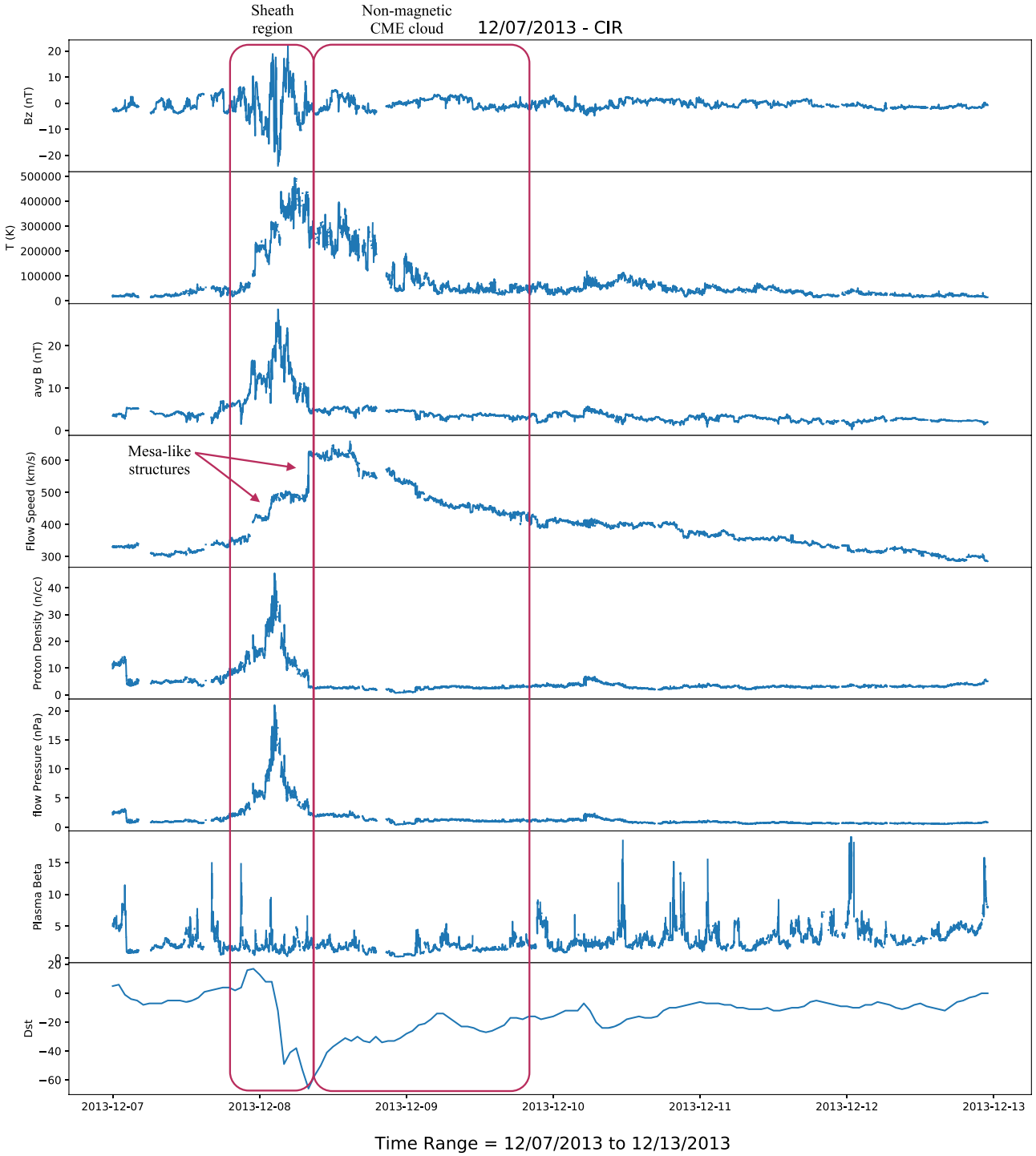

Figure 3. Solar wind at L1 indicating a CIR with B_z oscillating between southward (negative) and northward (positive) and flow speed exhibiting a mesa-like structure. There was indeed a CME that launched from the Sun with an initial speed of 1165 km s^{-1} and an expected arrival time of 1.5 days. The CME (nonmagnetic) signature follows the CIR in the flow speed profile as indicated by the arrows. The boxed regions depict the duration and properties of the CIR and CME as seen at L1.

We are confident that the above steps strongly ensure that the ICMEs correspond to their designated CME counterparts and no major interaction occurred in the inner heliosphere. Our results are summarized below.

4. Results

The total number of CMEs in the 2007–2017 period is more than 30,000. Among these, the number of halo-CMEs in the said time period is 292. Out of the 292 halo-CMEs, 206 occurred on the backside of the Sun or no ICME type signatures were seen near the Earth—these are not considered in our analysis. For all of the remaining 86 ICMEs, the axial magnetic field direction of the CME source on the Sun is determined using the chirality method as described in Section 2.

Out of the 86 CMEs that occurred from the solar side facing Earth, 63 have the same orientation at L1 as their filament counterpart had on the Sun. Of the remaining 23, 12 ICMEs

were such that they could not be classified as having a north or south component at L1 or at the Sun due to either low resolution images or ambiguity in ACE data. The remaining 11 events showed opposite configuration at L1 compared to that at the source region.

We summarize the reasons for nonclassification of the ambiguous 12 ICMEs as follows:

1. There are two ICMEs that are non-MC structures (ICMEs #11 and #199 in the catalog), hence their preference for orientation could not be determined.
2. Two ICMEs (#91 and #183) were tightly wound regions that produced jet-like features on the Sun; there were no filaments in these regions to identify the chirality and direction of the axis.
3. For one event (#43) the ICME signature was not observed at the expected time, perhaps because it did not reach Earth; its corresponding chirality sign and thus the axis direction also could not be determined because the flare occurred when the region was at the limb. The region was rotated to a later day to find the chirality but it was still very active and saturated, so no signatures could be seen.
4. #75 did not show any ICME signatures and #110 showed CIR type signatures.
5. One event (#121) showed signatures of three ICMEs, two showing negative and one showing positive B_z enhancements. On the Sun, there were three partial halo-CMEs in addition to the halo-CME within about three hours of each other, two of these regions have a southward and one has a northward pointing axis region.
6. Two events (#s 81 and 221) did not show much variation (signal within the solar wind) in B_z but only small variations are seen in B_x and B_y. The source region for #81 was southward pointing, but the CME originated from the west limb. It is possible that only a small portion of the ICMEs (for example, its flank) was seen by ACE. Also likely, the structure may have rotated in the interplanetary space which may explain the nondetection of the B_z enhancement.
7. One ICME (#272) showed short time signatures of southward and northward B_z. On the Sun, there was one halo and three partial halo CMEs that were produced on that day, hence it was not possible to determine the exact correlation for this ICME. In addition, the Dst index did not drop below −30 during this ICME and so it did not have much effect on Earth.
8. For ICME #239, the enhancement in Bz was positive at the expected arrival time. However, the corresponding CME originated at the west limb and another halo-CME (#240) occurred on the same day from a heliographic longitude of 40W that has a somewhat higher likelihood of affecting Earth (Gopalswamy et al. 2011). Thus we suspect that the observed signatures of #239 were actually due to #240.

Eleven ICMEs—12, 22, 94, 95, 112, 146, 147, 159, 257, 266, and 281 show opposite IMF B_z signatures than their filament counterparts. We confirm that no other strong and wide CMEs occurred close to the times of these CMEs. Because of this, we speculate that these ICMEs may have either rotated after the eruption or deflected due to encountering coronal holes or CIRs (Kay et al. 2017). Based on the above lists, we have 74 ICMEs out of which 63 show nonrotational behavior and 11 suggest rotational behavior. We present the results in the form of a confusion matrix (Ting 2017) or a truth table in Table 1 showing the number of northward and southward sources correlating with the number of northward and southward ICME B_zs. It is pertinent to give statistical quantities such as recall (a probability of detection or sensitivity) and precision (a success ratio; Ting 2011) for a classification such as ours where the same direction of IMF B_z and the CME source region acts as the classifier. Considering southward B_z as positive predictions, i.e., antialignment of Bz with respect to that of Earth's dipole field in which case geomagnetic storms will occur, we calculate a recall of 94.3% and a precision of 78.5% suggesting that a model algorithm will be required to improve the precision. This might be possible with more data. The higher recall suggests a lower number of false negative cases and hence the number of times an unnecessary precaution is taken will be very low.

Table 1
Distribution of Filaments

Filament Field → IMF Bz ↓	North	South
Northward	30	9
Southward	2	33

Note. Number of ICMEs = 74, Recall = 94.3%, Precision = 78.5%.

5. Discussion and Conclusions

This study has provided strong observational evidence that the north–south component of the axial field of solar chromospheric filaments and active regions obtained by assessing the chirality can be used effectively for determining the direction of the ICME magnetic fields at L1 and, by extension, for determining the geoeffectiveness of these CMEs. We determine the direction of the axial field of the filaments using chirality; however, we only consider the B_z component of the axial field (and then find whether it agrees with the B_z component of the ICME flux rope at L1). The other studies discussed here focus on the orientation of the axial field and not just B_z.

In their study, Marubashi et al. (2015) obtain the helicity of flux ropes at L1 using flux rope fitting methods and fit the axis of the flux rope onto the source region for filaments between 1996 and 2006 (our data covers from 2007 to 2017). They find that the PIL of the source region makes a similar angle as the flux rope at L1 within a range of about 25° for all cases in their data. They however do not obtain the direction of the axial field of the source region separate from the interplanetary flux rope measurements like we do. Similar to the above study, Yurchyshyn (2008) obtains the axis of the CME source using the method described in Yurchyshyn et al. (2001). They then fit ellipses to the shape of the halo-CME (LASCO images) to obtain the CME orientation angle at $2.5R_{\rm Sun}$ for 25 cases and find a very good correlation (95%) between the EIT arcade angles and the halo-CME axis but a 77% correlation between the halo-CME orientation and the MC orientation angles at L1; they suggest that the rest of the CMEs have rotated by more than 45°. We note that both of these studies are not inconsistent with our results.

Palmerio et al. (2018) have compared the orientation of the flux rope at L1 and that at the source using the method of chirality for 20 CMEs between 2010 and 2015 that could be

observed simultaneously by STEREO, SOHO, and SDO. Their analysis results in 55% of the cases being a match between the source and the in situ measurements of the ICME. Fifteen of their regions are common with ours and we find that we obtain the same filament axial field direction for 12 of the 15 cases. Eleven out of 15 ICME flux rope axial field component directions at L1, which were deduced from their flux rope types, match with our B_z sign. It is difficult to be certain about the mismatches in filament field directions because the methods used by them to find chirality (e.g., EUV sigmoids, magnetic tongues, etc.) are different from ours for some of their cases. The axial field direction is sensitive to chirality; if one determines the region is right chirality but is actually left, then the sign of the field direction would be just the opposite. Furthermore, our study on the relation between sigmoid shape and filament chirality (in preparation) suggests that there is no absolute relation between the two. The mismatches in the B_z component at L1 are attributed to the fact that we use the vertical component of the axial field at L1 and they use the total field using flux rope fitting methods. This as suggested in Palmerio et al. (2018) sometimes gives an opposite configuration. To compare the precision and recall metrics of their data, we derived the Bz component using the source "flux-rope type" for the filaments on the Sun and the "flux-rope type" was obtained by fitting methods at L1 (e.g., WNE would give a northward axial field direction). We calculate a precision and recall of about 66.6% and 72.7%, respectively, for their data. Ours is a somewhat better result but we do use a larger sample of events; as Palmerio et al. (2018) studied only 20 filaments, the difference in the percentages is likely due to the better statistical significance of our sample. Further comparison of the methods is of little meaning at this point as we believe that our method will be of use as a first step for obtaining the quick knowledge of effectiveness and the computational methods (like extrapolations and flux-rope fitting) for further determining the magnitude of the CME impact.

Bothmer & Schwenn (1998) compared the helicity of a set of quiescent filaments using the hemispheric helicity preference (Rust & Kumar 1994) with their ICME counterparts. They found a significant agreement in quiescent filaments to the rule (89%; a total of 9 filaments). Savani et al. (2015) also used the hemispheric helicity rule for obtaining the axis orientation for eight events but they warn that extra care must be taken while determining axis orientation of filaments that are between multiple active regions. Several statistical surveys on the hemispheric preference of helicity show varying degrees of compliance (for example, see HaiQing et al. 2009). In some of these studies (e.g., Martin et al. 1994), quiet regions show a higher degree of preference compared to the active regions. However, none of the studies show a 100% compliance with the hemispheric helicity rule indicating that independently obtaining the field direction at each source region is important. In order to avoid errors arising from exceptions in the hemispheric helicity rule and/or issues in disambiguation techniques, we have relied solely on filament observations and LOS magnetograms for obtaining the required parameters. We believe our method has performed well and has given reliable results. The human eye performs well in obtaining the chirality with images of reasonable resolution, but it is impractical to have human eyes analyze each and every filament. The advent of computer vision in solar physics is promising: automating filament chirality determination using machine-learning techniques (Martens et al. 2012; Aggarwal et al. 2018) will help in preparing computationally efficient and effective measures against severe space weather effects.

Knowing whether there will be a geomagnetic effect or not is of primary importance to start taking precautionary measures. However, precautionary measures during a false alarm and the resulting expenditures can be avoided with the method used in this paper. Furthermore, our method of determining the axial field direction is more quick and straightforward than computationally expensive methods such as force free extrapolations and determining helicity (Bothmer & Schwenn 1998; Yurchyshyn et al. 2001 etc.).

In the current study we consider only the north–south component of the axial magnetic field of the filament. This is deemed useful as a first step in omitting ICMEs that will not be geoeffective. However, it is necessary to know the exact, quantitative direction and strength to determine where an ICME might reconnect with the magnetosphere and its severity. Utilizing vector magnetograms to determine the exact orientation and further study the field in the corresponding flux ropes at L1 will be useful in determining their orientations. Active region filaments have fibrils and barbs that are smaller than the resolution limit of most available telescopes. Gosain & Brandenburg (2019) show that small scale magnetic fields emerging in active regions usually have opposite helicity compared to that in the already existing active region. Hence, analysis by looking at small filaments in active regions may lead to an incorrect assessment of their chirality. Ultra-high resolution spectropolarimetric instruments such as those on Daniel K. Inouye Solar Telescope (DKIST; Tritschler et al. 2016) will prove immensely useful in further understanding the filament magnetic field especially in active regions and the orientation of the barbs and fibrils adjacent to the filament spine.

The data set used for this study to determine ICME geoeffectiveness are by far the largest used, with 86 Earth-bound CMEs between 2007 and 2017. There are a few assumptions that this study has considered that can be improved. In reality, the CME travel time is not linear (acceleration and deceleration are not considered in calculating the expected arrival time, instead initial speed as calculated from LASCO observations is used) because of drag effects due to interaction with the solar wind, other CMEs, and CIRs. However, considering a qualitative estimate of the CME arrival time using the speed and acceleration information, almost all of the ICMEs were accounted for. Obtaining chirality with low resolution data is a challenge; we have attempted an unbiased analysis of the filament regions in this study to obtain the chirality. However, it is possible that, due to unavailability of high resolution data, some filaments may have been mistaken to be of opposite chirality (Martin 2015). However, we are certain that observationaly a correlation between CME and ICME orientations prevails.

The authors are sincerely thankful to the anonymous referee and to Dr. Manoulis Georgoulis for thoroughly reviewing the manuscript and for comments and suggestions that have considerably improved this manuscript. Hα data were provided by the Kanzelhöhe Observatory (KSO), University of Graz, Austria, and the National Solar Observatory (NSO) Global Oscillations Network Group (GONG). We are grateful to them and to J.H. King and N. Papatashvilli of Adnet Systems, NASA

GSFC, and CDAWeb for providing the interplanetary plasma data. We thank OMNIWeb for their effort in creating a common database for such parameters from various spacecraft. We thank the ACE instrument team and the ACE Science Center for providing the ACE data. We thank the CDAW team for putting together the CME and Halo-CME data set and providing it online. We extend our thanks to the SOHO/MDI and the EIT consortia for the data. SOHO is a project of international cooperation between ESA and NASA. We thank SDO/HMI and AIA teams for providing the reduced data. V. A. is grateful to Mrs. Sara Martin for her teaching and mentorship over the years and dedicates this paper to her. This work was supported by NASA grants NNX15AF39G and NNX15AQ61G S004-05-07-2019.

References

Aggarwal, A., Schanche, N., Reeves, K. K., Kempton, D., & Angryk, R. 2018, ApJS, 236, 15
Bothmer, V., & Schwenn, R. 1998, AnGeo, 16, 1
Brueckner, G. E., Howard, R. A., Koomen, M. J., et al. 1995, SoPh, 162, 357
Burlaga, L., Sittler, E., Mariani, F., & Schwenn, R. 1981, JGR, 86, 6673
Delaboudinière, J.-P., Artzner, G. E., Brunaud, J., et al. 1995, SoPh, 162, 291
Dungey, J. W. 1962, JPSJS, 17, 15
Forsyth, R. J., & Marsch, E. 1999, SSRv, 89, 7
Gopalswamy, N. 2009, in Climate and Weather of the Sun-Earth System (CAWSES)—Selected Papers from the 2007 Kyoto Symp., ed. T. Tsuda, R. Fujii, K. Shibata, & M. A. Geller (Tokyo: Terrapub), 77
Gopalswamy, N., Akiyama, S., Yashiro, S., Michalek, G., & Lepping, R. P. 2008, JASTP, 70, 245
Gopalswamy, N., Davila, J. M., St., Cyr, O. C., et al. 2011, JASTP, 73, 658
Gopalswamy, N., Yashiro, S., Michalek, G., et al. 2009, EM&P, 104, 295
Gosain, S., & Brandenburg, A. 2019, ApJ, 882, 80
HaiQing, X., Yu, G., & HongQi, Z. 2009, ScChG, 52, 1749
Hapgood, M. A. 1992, P&SS, 40, 711
Harvey, J. W., Bolding, J., Clark, R., et al. 2011, BAAS, 43, 17.45
Kay, C., Gopalswamy, N., Xie, H., & Yashiro, S. 2017, SoPh, 292, 78
Kilpua, E., Koskinen, H. E. J., & Pulkkinen, T. I. 2017, LRSP, 14, 5
Lemen, J. R., Title, A. M., Akin, D. J., et al. 2012, SoPh, 275, 17
Martens, P. C. H., Attrill, G. D. R., Davey, A. R., et al. 2012, SoPh, 275, 79
Martin, S. F. 1998, in IAU Coll. 167: New Perspectives on Solar Prominences 150, ed. D. F. Webb, B. Schmieder, & D. M. Rust (San Fransisco, CA: ASP), 419
Martin, S. F. 2015, ASSL, 415, 205
Martin, S. F., Bilimoria, R., & Tracadas, P. W. 1994, in Solar Surface Magnetism, NATO ASI Ser. C, ed. R. J. Rutten & C. J. Schrijver (Dordrecht: Kluwer), 303
Martin, S. F., Lin, Y., & Engvold, O. 2008, SoPh, 250, 31
Marubashi, K. 1997, GMS, 99, 147
Marubashi, K., Akiyama, S., Yashiro, S., et al. 2015, SoPh, 290, 1371
McComas, D. J., Bame, S. J., Barker, P., et al. 1998, SSRv, 86, 563
Müller, D., Fleck, B., Dimitoglou, G., et al. 2009, CSE, 11, 38
NASA CDAWeb Development Team 2019, CDAWeb: Coordinated Data Analysis Web, Astrophysics Source Code Library, ascl:1904.006
Palmerio, E., Kilpua, E. K. J., Möstl, C., et al. 2018, SpWea, 16, 442
Pizzo, V., Millward, G., Parsons, A., et al. 2011, SpWea, 9, 03004
Pötzi, W., Veronig, A. M., Riegler, G., et al. 2015, SoPh, 290, 951
Rust, D. M., & Kumar, A. 1994, SoPh, 155, 69
Savani, N. P., Vourlidas, A., Szabo, A., et al. 2015, SpWea, 13, 374
Scherrer, P. H., Bogart, R. S., Bush, R. I., et al. 1995, SoPh, 162, 129
Scherrer, P. H., Schou, J., Bush, R. I., et al. 2012, SoPh, 275, 207
Stone, E. C., Frandsen, A. M., Mewaldt, R. A., et al. 1998, SSRv, 86, 1
Ting, K. M. 2011, in Encyclopedia of Machine Learning, ed. C. Sammut & G. I. Webb (Boston, MA: Springer), 33
Ting, K. M. 2017, in Encyclopedia of Machine Learning and Data Mining, ed. C. Sammut & G. I. Webb (Boston, MA: Springer), 9
Tritschler, A., Rimmele, T. R., Berukoff, S., et al. 2016, AN, 337, 1064
Vourlidas, A., Lynch, B. J., Howard, R. A., & Li, Y. 2013, SoPh, 284, 179
Yurchyshyn, V. 2008, ApJL, 675, L49
Yurchyshyn, V. B., Wang, H., Goode, P. R., & Deng, Y. 2001, ApJ, 563, 381